On the short and long phosphorescence lifetimes of aromatic carbonyls

Saikat Mukherjee, Moumita Kar, Mansi Bhati, Xing Gao, Mario Barbatti

On the short and long phosphorescence lifetimes of aromatic carbonyls

Saikat Mukherjee,[1,a*] Moumita Kar,[1,b] Mansi Bhati,[2,c] Xing Gao,[3,d] Mario Barbatti[1,4,e*]

[1]*Aix Marseille University, CNRS, ICR, Marseille, France*
[2] *Department of Chemistry, University of Pennsylvania, Philadelphia, Pennsylvania 19104, USA*
[3] *School of Materials, Sun Yat-sen University, 518100 Shenzhen, Guangdong, China*
[4] *Institut Universitaire de France, 75231 Paris, France*

Corresponding authors: *SM: saikat.mukherjee@univ-amu.fr*
MB: mario.barbatti@univ-amu.fr, www.barbatti.org

[a]*ORCID: 0000-0002-0025-4735*
[b]*ORCID: 0000-0001-5728-4989*
[c]*ORCID: 0000-0002-8029-0516*
[d]*ORCID: 0000-0002-7726-2717*
[e]*ORCID: 0000-0001-9336-6607*

Abstract: This work applies theoretical and computational methods to investigate the relationship between phosphorescence lifetime and the electronic character of the lowest triplet state of aromatic carbonyls. A formal analysis of the spin-perturbed wave functions shows that phosphorescence is due to a direct spin-orbit coupling mechanism modulated by permanent dipoles when the T_1 minimum is $^3n\pi^*$. If the minimum is a totally symmetric $^3\pi\pi^*$, phosphorescence is due to an indirect spin-orbit coupling mechanism involving transition dipole moments with other excited states. The magnitude difference between permanent and transition dipoles leads to a much faster $^3n\pi^*$ phosphoresce than $^3\pi\pi^*$. These predictions were verified with phosphorescence lifetime simulations of benzaldehyde and its three derivatives in the gas phase employing a vertical approximation and the nuclear ensemble approaches. Both predict $^3n\pi^*$ emission within a few tens of milliseconds. While the vertical approach indicates a $^3\pi\pi^*$ emission within a few seconds, vibronic corrections bring this value down to about 200 ms.

Keywords: Phosphorescence, Organic chromophores, Benzaldehyde, Nuclear ensemble approach, Spin forbidden transitions, Selection rules

Version of record: S. Mukherjee, M. Kar, M. Bhati, X. Gao, M. Barbatti, **On the short and long phosphorescence lifetimes of aromatic carbonyls**, Theor. Chem. Acc. (2023). DOI: 10.1007/s00214-023-03020-w

1 Introduction

Since the 1960s, it has been well-established that the phosphorescence lifetime of aromatic carbonyl compounds is shorter for $^3n\pi^*$ than for $^3\pi\pi^*$ triplet minima [1, 2]. Harrigan and Hirota experimentally estimated that the ratio between those lifetimes should be of a factor of five or bigger for aromatic carbonyls of benzaldehyde type [3]. This difference between phosphorescence lifetimes is often experimentally employed to assign the triplet state character [3], and several papers discuss when this assignment may break due to vibronic couplings [4, 5]. Moreover, it is at the basis of strategies for designing efficient pure organic room-temperature phosphorescent chromophores [6]. Nevertheless, the reason for existing such a significant difference in the first place is not usually explicitly discussed.

Naturally, we may expect the shorter phosphorescence lifetime of the $^3n\pi^*$ compared to the $^3\pi\pi^*$ in aromatic carbonyls to be rooted in the symmetry of the Hamiltonian terms. Some excellent reference texts discuss this topic in general terms [7, 8] and applied to other heteroaromatic molecules [9, 10], but how this knowledge transfers to aromatic carbonyl compounds is not directly evident.

The reason for the phosphorescence lifetime difference is often considered to be related to the El-Sayed rule [11]. During the research for this article, we asked social networks what the cause of this phenomenon would be. The El-Sayed rule was the most common answer, indicating this explanation's popularity among the chemistry community. Nevertheless, despite exhaustive research, we could not locate any reference that convincingly showed how the El-Sayed rule would apply in this case. The closest we found was Olmsted and El-Sayed's analysis of BA phosphorescence [4]. They attributed the benzaldehyde's $^3n\pi^*$ phosphorescence to spin-orbit coupling (SOC) between the triplet $^3n\pi^*$ and the singlet $^1\pi\pi^*$ states, but, as we will discuss later, this seems not to be the case.

We perused 65 years of literature unsuccessfully searching for a theoretical analysis of phosphorescence lifetime in aromatic carbonyls. The only discussion we found is in the 1974 paper by Cheng and Hirota [12], in which all elements are laid out to address the problem. However, they did not explicitly discuss the difference in phosphorescence lifetimes, instead focusing on the vibronic couplings and zero-field splittings. Thus, we decided to fill this knowledge gap by surveying how molecular symmetry impacts phosphorescence from $^3n\pi^*$ and $^3\pi\pi^*$ in these molecules.

We show that the difference in the phosphorescence lifetimes is due to a selection rule related to (but more general than) the El-Sayed rule, controlling the coupling mechanism in each type of state. In particular, the lifetime difference occurs if the difference between the permanent dipole moments of S_0 and T_1 is significant and $^3\pi\pi^*$ is totally symmetric. We also show that it should strictly occur only for molecules attaining C_{2v} and D_2 symmetries, although it may occasionally be observed in other point groups. Finally, we discuss how vibronic effects impact the phosphorescence lifetimes.

The conventional approach to estimating the spontaneous emission lifetime is to compute transition dipole moments at the minimum of the source state and feed them to Fermi's golden rule [13].

However, when dealing with phosphorescence, the transition is spin-forbidden, rendering null transition dipole moments. This restriction is usually overcome by generating first-order spin-perturbed wave functions for the source and target states, which yields non-null transition dipole moments [7, 8, 14-17]. Our analysis was entirely based on this spin-perturbed procedure, which is straightforward to apply if SOC elements are available.

Phosphorescence can also have significant contributions from vibronic couplings arising from symmetry reduction during vibrational motion. Different methods are available to incorporate vibronic couplings into the simulations, such as the nuclear ensemble approach (NEA) [18], direct vibronic coupling [19], adiabatic Hessian [20], and vertical gradient [21]. Torres and co-authors recently compared them, and the interested reader may know more about the pros and cons of each one in their paper [22]. We particularly favor NEA, which we have been developing and applying for many years to simulate different spectrum types and generate initial conditions for dynamics [18, 23, 24].

NEA simulates steady-state and time-resolved spectra by performing an incoherent sum over independent transitions from different nuclear configurations [18]. These configurations are sampled to represent the nuclear wave function distribution in the source state (the lowest triplet state for phosphorescence). Standard NEA, however, does not include any information about the target state wave function (the ground state for emission spectra) [25]. Therefore, the band shape is entirely determined by the source-state features, and vibrational structures are neglected. Moreover, NEA has a high intrinsic cost of a few hundred single-point calculations, which can be alleviated using machine learning [26].

One advantage of employing NEA for phosphorescence analysis is that it allows decoupling perturbative terms acting in the symmetric structure from those paying a role through vibronic couplings. For example, Cheng and Hirota [12] included vibronic coupling terms directly in the perturbative expansion, making distinguishing each effect's origin difficult.

We implemented a strategy for simulating steady-state phosphorescence spectra with NEA to verify our formal analysis. The results are compared to the conventional vertical approximation. This initial work is restricted to TDDFT, but generalizing it to other methods is straightforward if SOC elements are available.

We simulated the vertical and NEA phosphorescence of four prototypical chromophores in the gas phase (see Figure 1): benzaldehyde (BA), 4-methylbenzaldehyde (MeBA), 4-methoxybenzaldehyde (MoBA), and 4-dimethylaminobenzaldehyde (DMABA). The small size of these molecules and the abundance of previous experimental [27-37] and theoretical [38-40] results for BA and its derivatives make them ideal for demonstrating the method. The motivation for choosing these molecules is that the functional groups in the series BA, MeBA, MoBA, and DMABA have an increasing electron donor character, stabilizing the $^3\pi\pi^*$ state, as well known [41]. Thus, we can probe phosphorescence under different relative energies between the $^3n\pi^*$ and $^3\pi\pi^*$ states.

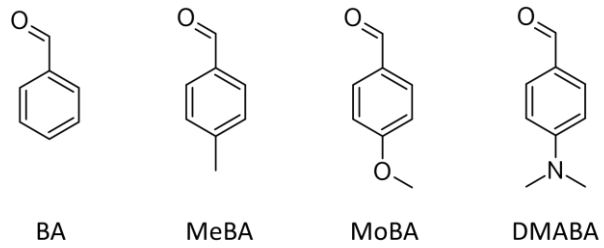

Figure 1. Benzaldehyde (BA) 4-methylbenzaldehyde (MeBA), 4-methoxybenzaldehyde (MoBA), and 4-dimethylaminobenzaldehyde (DMABA).

The lowest triplet electronic state (T_1) of BA can be directly photoexcited [27], activated via collisional processes [28], or, more usually, populated after photoabsorption into the singlet manifold [29-31]. In the latter case, the efficiency of singlet→triplet intersystem crossing is near unity [29, 32]. Thus, BA has weak fluorescence and shows phosphorescence either in a solid matrix [33] or in the gas phase [27, 30, 31, 42]. At zero pressure, the phosphorescence takes between 2 and 4.3 ms [29, 30]. The phosphorescence quantum yield is 0.60, while the $T_1 \rightarrow S_0$ intersystem crossing quantum yield is 0.40. The phosphorescence quantum yield decreases on excitation from S_0 to S_1, S_2, and S_3 states, indicating competitive relaxation pathways through nonradiative processes in each excited state. Moreover, a triplet excited state (T_2) also plays a vital role in quenching S_2 and S_3 states [31]. A monotonic decrease of the quantum yield for BA phosphorescence with increasing excitation wavenumber is also reported confirming the complex decay mechanism [30].

Studies about the phosphorescence of the other derivatives are sparser [1, 3, 35, 43, 44]. A fascinating case is MoBA, which phosphoresces within 1 ms in vapor [43], but within 120 ms within a rigid glass at 77 K.

All BA derivatives investigated in this work are small molecules with highly structured spectra. As mentioned, NEA entirely neglects those vibrational structures, only delivering a smoothed band shape. Despite this limitation, NEA yields valuable information, particularly the lifetime, beyond the vertical approximation. Moreover, NEA is intended as a practical methodology aiming at medium to large molecules, where such vibrational structures become less prominent.

2 Theory

For phosphorescence, the NEA differential emission rate (dimensionless) from T_1 into S_0 is [18]

$$\Gamma_{rad}(E) = \frac{2\alpha}{m_e c^2}\left[1 - H(E - h\nu_a)\right]\frac{1}{N_p}\sum_{n}^{N_p}\Delta E_{10}(\mathbf{R}_n)^2\left|\tilde{f}_{10}(\mathbf{R}_n)\right| w_s\left(E - \Delta E_{10}(\mathbf{R}_n), \delta\right) \qquad (1)$$

where α is the fine-structure constant, m_e is the electron mass, c is the speed of light. $H(E - h\nu_a)$ is the Heaviside step function, ensuring that the emission energy E is smaller than the excitation energy $h\nu_a$. N_p is the total number of geometries $\mathbf{R}_n$ in the ensemble. ΔE_{10} is the transition energy between

T_1 and S_0 computed for each geometry $\mathbf{R}_n$. $\tilde{f}_{10}$ is the oscillator strength between the spin-perturbed $\tilde{T}_1$ and $\tilde{S}_0$ states for each geometry. Its calculation is discussed later in this section. w_s is a normalized sharp line shape (a Gaussian function, for instance) centered at ΔE_{10} and with width δ. The nuclear geometries $\mathbf{R}_n$ are sampled with a Wigner distribution for the quantum harmonic oscillator at the T_1 minimum.

The phosphorescence rate $\kappa_{rad}^{(NEA)}$ and phosphorescence lifetime $\tau_{rad}^{(NEA)}$ are

$$\kappa_{rad}^{(NEA)} = \frac{1}{\tau_{rad}^{(NEA)}} = \frac{1}{\hbar}\int \Gamma_{rad}\left(E\right) dE \tag{2}$$

For comparison, the vertical approximation for the phosphorescence rate and lifetime is

$$\kappa_{rad}^{(VER)} = \frac{1}{\tau_{rad}^{(VER)}} = \frac{2\alpha}{\hbar m_e c^2}\Delta E_{10}\left(\mathbf{R}_{T_1\min}\right)^2 \left|\tilde{f}_{10}\left(\mathbf{R}_{T_1\min}\right)\right| \tag{3}$$

In Eqs. (1) and (3), the oscillator strength between pure-spin T_1 and S_0 is null. However, due to SOC, the singlet states contain some triplet state character, and at the same time, the T_1 state is contaminated by singlet wave functions [8, 14-16]. In first-order perturbation theory, the spin-perturbed states are [8, 16]

$$\left|\tilde{S}_0\right\rangle = \left|S_0\right\rangle + \sum_{K}^{\{\text{triplets}\}}\sum_{\alpha}\frac{\left\langle T_K^{(\alpha)}\left|\hat{H}^{SO}\right|S_0\right\rangle}{{}^1E_0 - {}^3E_K}\left|T_K^{(\alpha)}\right\rangle \tag{4}$$

and

$$\left|\tilde{T}_1^{(\alpha)}\right\rangle = \left|T_1^{(\alpha)}\right\rangle + \sum_{L}^{\{\text{singlets}\}}\frac{\left\langle S_L\left|\hat{H}^{SO}\right|T_1^{(\alpha)}\right\rangle}{{}^3E_1 - {}^1E_L}\left|S_L\right\rangle \tag{5}$$

In Eq. (4), the sums run over the adiabatic triplet states K with energy ${}^3E_K$ and wave function $\left|T_K^{(m)}\right\rangle$ and over the triplet sublevels α. In Eq. (5), the sum runs over the adiabatic singlet states L with energy ${}^1E_L$ and wave function $\left|S_L\right\rangle$. $\hat{H}^{SO}$ denotes the SOC operator.

The transition dipole moment is

$$\begin{aligned}\tilde{\boldsymbol{\mu}}_{10}^{(\alpha)} &\equiv \left\langle \tilde{T}_1^{(\alpha)}\left|\hat{\boldsymbol{\mu}}\right|\tilde{S}_0\right\rangle \\ &= \sum_{L}^{\{\text{singlets}\}}\frac{\left\langle T_1^{(\alpha)}\left|\hat{H}^{SO}\right|S_L\right\rangle}{{}^3E_1 - {}^1E_L}\left\langle S_L\left|\hat{\boldsymbol{\mu}}\right|S_0\right\rangle + \sum_{K}^{\{\text{triplets}\}}\frac{\left\langle T_K^{(\alpha)}\left|\hat{H}^{SO}\right|S_0\right\rangle}{{}^1E_0 - {}^3E_K}\left\langle T_1\left|\hat{\boldsymbol{\mu}}\right|T_K\right\rangle\end{aligned} \tag{6}$$

where $\hat{\boldsymbol{\mu}}$ is the dipole moment operator and we used $\left\langle S_L\left|\hat{H}^{SO}\right|T_1^{(\alpha)}\right\rangle^* = \left\langle T_1^{(\alpha)}\left|\hat{H}^{SO}\right|S_L\right\rangle$. We can rewrite the transition dipole moment as

$$\tilde{\boldsymbol{\mu}}_{10}^{(\alpha)} = \frac{\left\langle \mathrm{T}_1^{(\alpha)} \middle| \hat{H}^{SO} \middle| \mathrm{S}_0 \right\rangle}{{}^3E_1 - {}^1E_0}\left[\left\langle \mathrm{S}_0 \middle| \hat{\boldsymbol{\mu}} \middle| \mathrm{S}_0 \right\rangle - \left\langle \mathrm{T}_1 \middle| \hat{\boldsymbol{\mu}} \middle| \mathrm{T}_1 \right\rangle\right] + \sum_{L\neq 0}^{\{\text{singlets}\}} \frac{\left\langle \mathrm{T}_1^{(\alpha)} \middle| \hat{H}^{SO} \middle| \mathrm{S}_L \right\rangle}{{}^3E_1 - {}^1E_L}\left\langle \mathrm{S}_L \middle| \hat{\boldsymbol{\mu}} \middle| \mathrm{S}_0 \right\rangle + \sum_{K\neq 1}^{\{\text{triplets}\}} \frac{\left\langle \mathrm{T}_K^{(\alpha)} \middle| \hat{H}^{SO} \middle| \mathrm{S}_0 \right\rangle}{{}^1E_0 - {}^3E_K}\left\langle \mathrm{T}_1 \middle| \hat{\boldsymbol{\mu}} \middle| \mathrm{T}_K \right\rangle \quad (7)$$

evidencing S_0 and T_1 permanent dipole moments in the first term.

Each of the three terms on the right side of Eq. (7) corresponds to a distinct coupling mechanism contributing to the transition dipole moment. The first term is a direct SOC between T_1 and S_0 modulated by these states' permanent dipoles (direct SOC mechanism):

$$\mathrm{T}_1 \overset{SOC,\mu_P}{\leftrightarrow} \mathrm{S}_0$$

In the second term, T_1 couples via spin-orbit to the S_L excited singlet states, then those singlet states couple to S_0 via transition dipole (indirect SOC-dipole mechanism):

$$\mathrm{T}_1 \overset{SOC}{\leftrightarrow} \mathrm{S}_L \overset{\mu_T}{\leftrightarrow} \mathrm{S}_0$$

Finally, the third term couples T_1 to the excited T_K triplet states via transition dipole, and then these triplet states couple to S_0 via SOC (indirect dipole-SOC mechanism):

$$\mathrm{T}_1 \overset{\mu_T}{\leftrightarrow} \mathrm{T}_K \overset{SOC}{\leftrightarrow} \mathrm{S}_0$$

To get the oscillator strength, we compute the mean transition dipole moment squared

$$\tilde{\mu}_{10}^2 = \frac{1}{3}\sum_{\alpha}\left|\tilde{\boldsymbol{\mu}}_{10}^{(\alpha)}\right|^2 \quad (8)$$

Finally, the oscillator strength is [13]

$$\tilde{f}_{10} = \frac{2m_e}{3\hbar^2 e^2}\Delta E_{10}\tilde{\mu}_{10}^2 \quad (9)$$

3 Computational details

The NEA phosphorescence spectrum [Eq. (1)] was simulated with 1000 geometries sampled from a quantum harmonic oscillator Wigner distribution in the T_1 state taking δ = 0.05 eV. For each geometry, the oscillator strength between $\tilde{\mathrm{T}}_1$ and $\tilde{\mathrm{S}}_0$ was computed with Eq. (9). The perturbative expansion [Eqs. (4) and (5)] included 20 singlet and 20 triplet states. S_0 is determined with density functional theory (DFT) with the B3LYP functional [45] and the 6-31G(d,p) basis set [46]. All other states were computed with linear-response time-dependent DFT (TDDFT) [47], with triplet states treated as excitations of the singlet reference.

Supplementary calculations were done with TDDFT with the CAM-B3LYP [48] and ωB97X [49] functionals. The results with TD-B3LYP were systematically superior, particularly predicting the ^{3}nπ*/^{3}ππ* energy splitting in MeBA and MoBA in excellent agreement with the experiments [35, 44]. Moreover, despite multiple attempts, we have not found the ^{3}nπ* minimum for BA and MeBA with TD-ωB97X, for which T_1 was always ^{3}ππ*. With TD-CAM-B3LYP, the T_1 optimization of BA was unsuccessful, systematically overstretching the carbonyl group and yielding negative excitations. These results are in line with those reported by Sears et al.[50], who demonstrated that the large amount of Hartree-Fock exchange in range-separated functionals could degrade TDDFT predictions of triplet states in π-conjugated molecules. Although the Tamm-Dancoff approximation could alleviate these problems, we decided to limit our simulations to TDDFT with B3LYP.

In TDDFT, the $\left|S_L\right\rangle$ and $\left|T_K^{(m)}\right\rangle$ wave functions can be written as single excitations of the Kohn-Sham ground-state singlet determinant as described in Ref. [51]. SOC was determined with a single-electron Breit-Pauli operator with an effective charge approximation (BP1e-eff) [51, 52].

We implemented the calculation of the oscillator strengths in a new version of PySOC [51], which calls Gaussian 16 [53] for TDDFT calculations, and MolSOC [54] to provide atomic integrals for SOC calculations. The NEA calculations were done with Newton-X [24], which we interfaced with PySOC, to deliver all results in a simple workflow. Technical details of how the transition dipole elements are computed in the frame of TDDFT are given in SI-1.

The convergence of the first-order perturbative approach was tested for the ^{3}nπ* T_1 minimum geometry of BA (vertical emission) by varying the number of states used in Eq. (6). The results for the oscillator strength [Eq. (9)] and vertical phosphorescence lifetime [Eq. (3)] are presented in Table 1, indicating a reasonable convergence is achieved for 20 triplet and 20 singlet states.

Table 1. Convergence of the perturbative treatment as a function of the number of singlet and triplet states considered. The zero-order T_1 vertical excitation energy is 2.336 eV.

N_{states}	Oscillator Strength ($\times 10^{-7}$)	Lifetime (ms)
2	2.90	15
5	0.65	65
10	1.05	40
15	1.26	33
20	1.09	39
25	1.09	39
30	1.13	38
35	1.12	38
40	1.13	38
45	1.11	38
50	1.10	38

4 Results

4.1 Electronic states of benzaldehyde

BA is perfectly planar in the ground singlet and triplet states (S_0 and T_1) and low-lying singlet excited states (S_1 and S_2). It has a global T_1 minimum with a $^3n\pi^*$ character. With TD-B3LYP, we could neither find a $^3\pi\pi^*$ minimum in T_1 nor T_2. Nevertheless, a $^3\pi\pi^*$ stationary structure lies 0.09 eV above the $^3n\pi^*$ minimum. We will refer to this structure as $^3\pi\pi^*$ T_1 minimum, but note that it has an imaginary frequency of 171*i* cm^{-1}. State energies at the S_0 and S_1 minima are given in Table 2. Energies at the T_1 and T_2 minima are in Table 3. The electronic excitations and molecular orbitals to identify the state characters are given in the SI-2.

Figure 2 shows the linearly interpolated potential energy profiles between the $^3n\pi^*$ and $^3\pi\pi^*$ minima. Because the $^3n\pi^*$ minimum is more stable and should couple to the ground state more strongly than $^3\pi\pi^*$, we will focus on this minimum.

The most notable geometrical difference between S_0 and T_1 $^3n\pi^*$ minima lies in the carbonyl angle (O-C7-H), which decreases by almost 10° in $^3n\pi^*$ compared to S_0. The carbonyl bond length (C7-O) increases by 0.1 Å from S_0 to $^3n\pi^*$. On the other hand, the bond between carbonyl and ring carbon (C1-C7) also decreases by about 0.1 Å from S_0 to $^3n\pi^*$. The ring C-C and C-H distances remain approximately the same in both structures. The relevant internal coordinates in S_0, S_1, and T_1 minima are compared with previously reported experimental and theoretical data in SI-3. The vertical excitation energies at S_0, S_1, and T_1 minima of benzaldehyde are compared with previous results in SI-4. Generally, the present results calculated with the TD-B3LYP agree reasonably well with the reported CASPT2 energies [55]. However, the energies of the triplet manifold reported in Ref. [40] are closer to the CASPT2 ones than in the present case. The discrepancies seem to be due to our treatment of the triplets as excitations of the singlet reference.

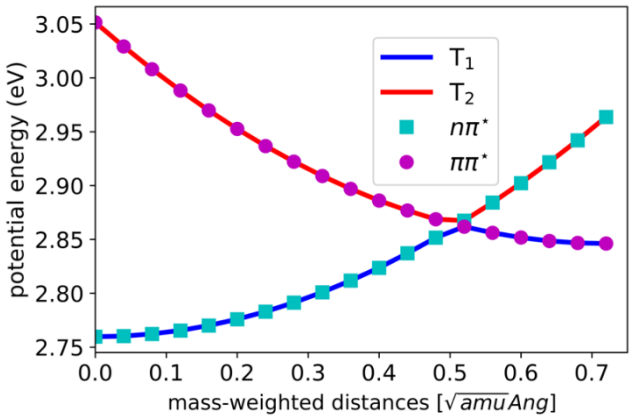

Figure 2. Potential energy scan of T_1, T_2 adiabatic states and $^3n\pi^*$, $^3\pi\pi^*$ diabatic states at the linear interpolation coordinates between $^3n\pi^*$ and $^3\pi\pi^*$ minima geometries of benzaldehyde. The horizontal axis is the mass-weighted distance from the $^3n\pi^*$ minimum geometry.

4.2 Electronic states of the BA derivatives

The energetics of the BA derivatives are given in Table 2 and Table 3. The S_1 $^1n\pi^*$ minimum of MeBA and MoBA is above the $^3\pi\pi^*$ state by 0.35 and 0.45 eV, respectively, being a door for populating the triplet manifold via an intersystem crossing. In DMABA, this gap is 0.64 eV, making ISC less likely according to the El-Sayed rule [56].

Table 2. Ground and excitation energies (eV) at the S_0 and S_1 minima of BA and its derivatives calculated with TD-B3LYP/6-31G(d,p). The state character is also indicated. The excitation energies are relative to the ground-state minimum energy.

	BA		MeBA		MoBA		DMABA	
State	S_0 min	S_1 min ($^1n\pi^*$)	S_0 min	S_1 min ($^1n\pi^*$)	S_0 min	S_1 min ($^1n\pi^*$)	S_0 min	S_1 min ($^1n\pi^*$)
S_0	0.00	0.40	0.00	0.41	0.00	0.41	0.00	0.42
T_1	3.12 ($^3n\pi^*$)	2.77 ($^3n\pi^*$)	3.15 ($^3n\pi^*$)	2.80 ($^3n\pi^*$)	3.16 ($^3\pi\pi^*$)	2.87 ($^3n\pi^*$)	2.88 ($^3\pi\pi^*$)	2.82 ($^3\pi\pi^*$)
T_2	3.30 ($^3\pi\pi^*$)	3.05 ($^3\pi\pi^*$)	3.23 ($^3\pi\pi^*$)	3.01 ($^3\pi\pi^*$)	3.23 ($^3n\pi^*$)	2.98 ($^3\pi\pi^*$)	3.27 ($^3n\pi^*$)	2.92 ($^3n\pi^*$)
S_1	3.68 ($^1n\pi^*$)	3.33 ($^1n\pi^*$)	3.70 ($^1n\pi^*$)	3.36 ($^1n\pi^*$)	3.78 ($^1n\pi^*$)	3.43 ($^1n\pi^*$)	3.81 ($^1n\pi^*$)	3.46 ($^1n\pi^*$)
S_2	4.78 ($^1\pi\pi^*$)	4.97 ($^1\pi\pi^*$)	4.77 ($^1\pi\pi^*$)	4.99 ($^1\pi\pi^*$)	4.81 ($^1\pi\pi^*$)	5.03 ($^1\pi\pi^*$)	4.30 ($^1\pi\pi^*$)	4.58 ($^1\pi\pi^*$)

Table 3. Ground and excitation energies (eV) at the lowest $^3n\pi^*$ and $^3\pi\pi^*$ triplet minima of BA and its derivatives calculated with TD-B3LYP/6-31G(d,p). The state character is also indicated. In BA, MeBA, and MoBA, both minima are T_1. In DMABA, they are T_1 and T_2. The excitation energies are relative to the ground-state minimum energy.

	BA		MeBA		MoBA		DMABA	
State	T_1 min ($^3n\pi^*$)	T_1 min ($^3\pi\pi^*$)	T_1 min ($^3n\pi^*$)	T_1 min ($^3\pi\pi^*$)	T_1 min ($^3\pi\pi^*$)	T_1 min ($^3n\pi^*$)	T_1 min ($^3\pi\pi^*$)	T_2 min ($^3n\pi^*$)
S_0	0.42	0.61	0.42	0.52	0.43	0.42	0.28	0.43
T_1	2.76 ($^3n\pi^*$)	2.85 ($^3\pi\pi^*$)	2.78 ($^3n\pi^*$)	2.79 ($^3\pi\pi^*$)	2.81 ($^3\pi\pi^*$)	2.86 ($^3n\pi^*$)	2.65 ($^3\pi\pi^*$)	2.83 ($^3\pi\pi^*$)
T_2	3.05 ($^3\pi\pi^*$)	2.96 ($^3n\pi^*$)	3.00 ($^3\pi\pi^*$)	3.01 ($^3n\pi^*$)	3.05 ($^3n\pi^*$)	2.99 ($^3\pi\pi^*$)	3.09 ($^3n\pi^*$)	2.91 ($^3n\pi^*$)
S_1	3.34 ($^1n\pi^*$)	3.52 ($^1n\pi^*$)	3.36 ($^1n\pi^*$)	3.55 ($^1n\pi^*$)	3.59 ($^1n\pi^*$)	3.43 ($^1n\pi^*$)	3.61 ($^1n\pi^*$)	3.47 ($^1n\pi^*$)
S_2	4.95 ($^1\pi\pi^*$)	5.07 ($^1\pi\pi^*$)	4.97 ($^1\pi\pi^*$)	4.99 ($^1\pi\pi^*$)	4.87 ($^1\pi\pi^*$)	5.03 ($^1\pi\pi^*$)	4.38 ($^1\pi\pi^*$)	4.58 ($^1\pi\pi^*$)

The most prominent feature in the state levels of BA and its derivatives is the relative energy gap between $^3n\pi^*$ and $^3\pi\pi^*$ states. In the sequence of increasing electron donation strength –H < –CH_3 < –OCH_3 < –$N(CH_3)_2$, the $^3n\pi^*$ state is destabilized while the $^3\pi\pi^*$ state is stabilized, as shown in Figure 3. All four species have a $^3n\pi^*$ and a $^3\pi\pi^*$ triplet minimum. The lowest triplet minimum in BA and MeBA is $^3n\pi^*$. In MoBA and DMABA, the lowest minimum is $^3\pi\pi^*$. The inversion occurs around MeBA, where the two minima are nearly degenerated, with $^3n\pi^*$ only 0.01 eV more stable than $^3\pi\pi^*$. This result nicely agrees with the measurements reported in Ref. [35]. In MoBA, the $^3\pi\pi^*$ minimum is lower than the $^3n\pi^*$ minimum by 0.05 eV, also in excellent agreement with the experimental estimates between 0.04 and 0.11 eV [44]. For BA, MeBA, and MoBA, both $^3n\pi^*$ and $^3\pi\pi^*$ minima are in T_1. In DMABA, the $^3n\pi^*$ minimum is in T_2.

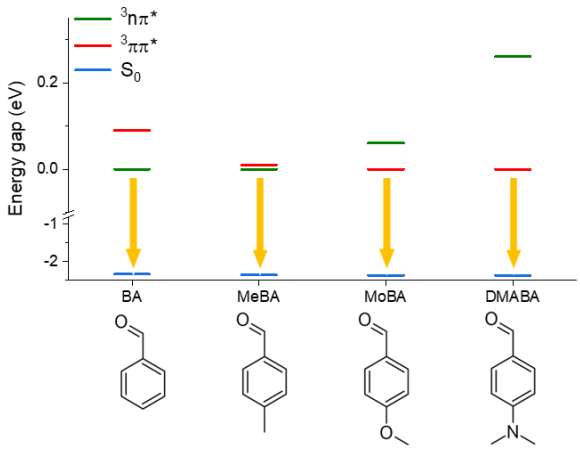

Figure 3. Energy gaps between S_0, $^3n\pi^*$, and $^3\pi\pi^*$ states in BA and derivatives. The lowest triplet state is set to zero, and the arrow indicates the vertical gap to S_0 computed at this triplet minimum. For BA, MeBA, and MoBA, the green and red levels correspond to the energy gap between the two T_1 minima. For DMABA, those two levels indicate the adiabatic energy gap between T_1 and T_2 minima.

4.3 BA phosphorescence spectrum

It is out of the scope of this paper to discuss the photophysics of BA until T_1 is populated. The reader interested in this aspect may check Ref. [40]. Here, our focus is the phosphorescence simulation. Thus, we assumed the $^3n\pi^*$ T_1 minimum is prepared at its vibrational ground state. Under this condition, the simulated BA phosphorescence spectrum in the gas phase is shown in Figure 4. It is compared with the experimental phosphorescence spectrum in vapor [57]. The theoretical spectrum shows no vibrational structure as expected for NEA and is redshifted due to the TDDFT treatment.

The area under the phosphorescence spectrum in terms of Γ_{rad} does not represent quantum yield but a lifetime. Employing Eq. (2), we obtain $\tau_{rad} = 46 \pm 1$ ms, a little longer than the vertical value computed at the T_1 minimum, 39 ms. Both values are above the experimental phosphorescence lifetime, which lies between 2 and 4.3 ms, depending on the setup [29, 30]. The only other theoretical estimate of the phosphorescence lifetime is by Ou and Subotnik [40], 1.81 ms. Their

calculation is equivalent to our vertical lifetime [Eq. (3)] with the $^3n\pi^* \rightarrow S_0$ transition calculated at TDDFT with the ωB97X functional, but we have not been able to determine the reason for the difference between our results. All these values are summarized in Table 4.

Table 4. Theoretical and experimental phosphorescence lifetime of benzaldehyde.

	k (s^{-1})	τ (ms)	Reference
Theory			
k_P: NEA	22	46 ± 1	Present work
k_P: Vertical emission	26	39	Present work
k_P: Vertical emission	553	1.81	[40]
Experimental (*at zero pressure*)			
k_P: $S_0 \rightarrow S_1(n\pi^*)$ 0-0 (3.34 eV)	235 ± 19	4.3 ± 0.3	[29]
k_0: $S_0 \rightarrow S_1(n\pi^*)$ 0-0 (3.34 eV)	392 ± 24	2.6 ± 0.2	[29]
k_0: $S_0 \rightarrow T_1(n\pi^*)$ (3.11 – 3.15 eV)	1410	0.712	[27]
k_P: $S_0 \rightarrow S_2$ (4.37, 4.49 eV)	500	2.0	[30]
k_0: $S_0 \rightarrow S_2$ (4.37, 4.49 eV)	690	1.5	[30]
k_0: 9-eV e^--impact, 3.12-eV emission	600	1.7	[28]
k_0: 9-eV e^--impact, 3.32-eV emission	1300	0.8	[28]

Many experimental results are available for benzaldehyde (see Table 4), which may lead to misunderstandings regarding which values we should take for comparison with theory. Two types of reaction rates are reported—the phosphorescence rate (k_P) and decay rate (k_0). The relation between them is [29]

$$k_p = k_0 - k_{ISC} = \Phi_P k_0 \qquad (10)$$

where k_{ISC} is the nonradiative intersystem crossing rate, and Φ_P is the phosphorescence quantum yield. Brühlmann et al. [29] obtained the phosphorescence lifetime by measuring the spectrally integrated T_1 decay following the $S_0 \rightarrow S_1$ excitation. This decay contains information on radiative and nonradiative components, and they report both k_P and k_0. Similarly, Hirata and Lim reported radiative and nonradiative decay rates [30]. In turn, Biron and Longin [27] and Inoue and Ebara [28] fitted the phosphorescence intensity signal. However, they did not explicitly consider nonradiative components. Thus, their reported rate should correspond to k_0. From the theory perspective, rates computed with either Eq. (2) or (3) must be exclusively compared with k_P.

Our estimate of BA phosphorescence lifetime, 46 ms (Table 4), is based on a Wigner distribution at the ground vibrational T_1 state. Thus, it should be compared to the lifetime measured under similar conditions, phosphorescence following excitation into T_1. Experimentally, BA phosphorescence

lifetime after S_2 excitation is 2 ms [30]. It increases to 4.3 ms for BA excited at S_1 [29]. These values may imply that the phosphorescence lifetime after excitation into T_1 (which is lower than S_1) may be longer than 4.3 ms, but unfortunately, such an experimental result is not available. Compared to the available experiments, our value (46 ms) seems to overestimate the phosphorescence lifetime. The reason for this overestimation seems to be connected to the computational level we used. Although TD-B3LYP yielded excellent results for the triplet states (as discussed in Section 3), the relative energy between triplet and singlet states have significant deviations, as we can see in the simulated spectrum in Figure 4. The theoretical spectrum is redshifted by about 0.7 eV. Furthermore, both SOCs and transition dipole moments were computed with auxiliary multi-electron wave functions [58, 59]. The accuracy of such approaches has not yet been fully gauged, and it may be a source of errors in estimating the phosphorescence lifetimes. Despite the overestimation, we shall see that the computed phosphorescence lifetimes deliver a satisfactory qualitative picture for the differences between $^3n\pi^*$ and $^3\pi\pi^*$ emissions.

4.4 Phosphorescence of the BA derivatives

The NEA phosphorescence spectrum of BA and derivatives is shown in Figure 4. For MeBA and MoBA, we computed the spectrum at the two T_1 minima, but only the one at the lowest minimum is given in the figure. The other offers similar results, as we shall discuss. The integral of these spectra [Eq. (2)] yields the phosphorescence lifetimes, which are collected in Table 5. The vertical phosphorescence lifetimes, computed for the T_1 minimum geometry with Eq. (3), are also reported in the table.

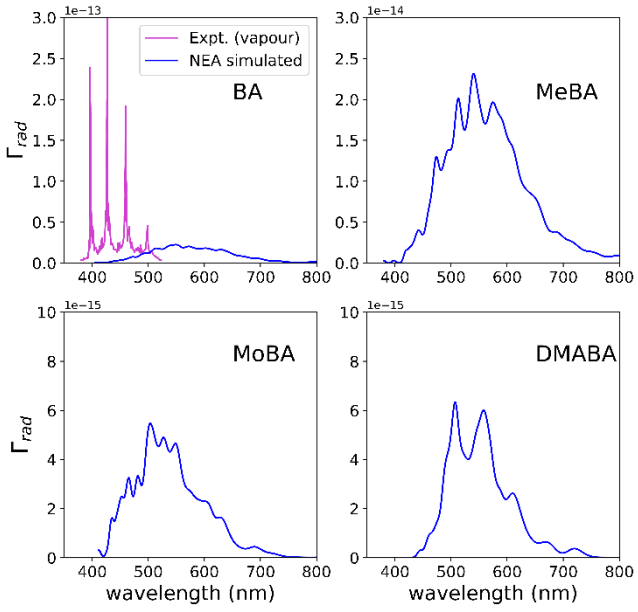

Figure 4. BA, MeBA, MoBA, and DMABA phosphorescence spectra in the gas phase simulated with NEA. Experimental results for BA from Ref. [57] normalized to have the same area as the simulation.

The phosphorescence lifetime of BA is discussed in Section 4.3. For all molecules, the vertical phosphoresce lifetime is between tens of ms for $^3n\pi^*$ emission and grows to several seconds for $^3\pi\pi^*$ emission (Table 5). This significant difference reduces when the vibronic coupling is incorporated via NEA. The $^3n\pi^*$ emission lifetime is slightly elongated to values between 46 and 75 ms. Still, the $^3\pi\pi^*$ emission lifetime is reduced up to a factor of 50 in DMABA, and all molecules show $^3\pi\pi^*$ phosphorescence within approximately 200 ms. The reason for these differences is discussed in Section 5.1.

Table 5. Phosphorescence lifetime of BA derivatives in vapor simulated with the vertical approximation and NEA.

		Phosphorescence lifetime (ms)	
T_1 minimum	Molecule	Vertical	NEA
$^3n\pi^*$	BA	39	46 ± 1
	MeBA	38	47 ± 1
	MoBA	61	75 ± 1
$^3\pi\pi^*$	MeBA	8380	217 ± 3
	MoBA	6870	214 ± 3
	DMABA	11530	231 ± 4

Unlike BA, for which experimental data is abundant, for the BA derivatives, the only available information about phosphorescence lifetime is for MoBA. MoBA in vapor has a lifetime of ~1 ms or less, obtained by indirect inference and assigned to the $^3n\pi^*$ emission in Ref. [43]. In a 77-K glass, the measured phosphorescence lifetime of MoBA is much longer, about 120 ms, and has been assigned to $^3\pi\pi^*$ emission [43, 57], indicating that the glass quenches the $^3n\pi^*$ emission. Our NEA values, 75 ms for $^3n\pi^*$ and 214 ms for $^3\pi\pi^*$ (Table 5), qualitatively capture the difference between the emission from the two states.

5 Discussion

5.1 Origins of the fast and slow phosphorescence

This section addresses why phosphorescence is faster from $^3n\pi^*$ than $^3\pi\pi^*$ states in aromatic carbonyls. We will take BA as an example and focus our discussion on $T_1 \rightarrow S_0$ phosphorescence. First, we must remember that state symmetry should consider both the usual symmetry representation of the spatial wave function and the symmetry representation generated by the spin wave function. The spin wave function of the singlet state always transforms as the totally symmetric representation of the group (Γ_1), while the spin wave function Cartesian components belong to the representations generated by the R_x, R_y, and R_z rotations [7]. Thus,

$$\Gamma\left(\left|T_K^{(\xi)}\right\rangle\right) = \Gamma\left(\left|T_K\right\rangle\right)\Gamma\left(R_\xi\right) \tag{11}$$

where $\Gamma(\ )$ gives the irreducible representation.

$T_1 \rightarrow S_0$ phosphorescence will be symmetry allowed if two selection rules are satisfied. The first one concerns the SOC terms appearing in the singlet-triple transition dipole moment, Eq. (7):

$$\Gamma\left(\left\langle S_L \left| \hat{H}^{SO} \right| T_K^{(\xi)} \right\rangle\right) = \Gamma_1 \tag{12}$$

Because $\Gamma\left(\hat{H}^{SO}\right) = \Gamma_1$, Eq. (12) simplifies to

$$\Gamma\left(\left|S_L\right\rangle\right) = \Gamma\left(\left|T_K^{(\xi)}\right\rangle\right) \tag{13}$$

Note that, for convenience, we wrote the states in terms of the Cartesian components ξ instead of the magnetic quantum number *m*, which is actually employed in our program. The transformation between the two representations is [8]

$$\begin{aligned}
\left|T^{(x)}\right\rangle &= \frac{1}{\sqrt{2}}\left(\left|T^{(-1)}\right\rangle - \left|T^{(+1)}\right\rangle\right) \\
\left|T^{(y)}\right\rangle &= \frac{i}{\sqrt{2}}\left(\left|T^{(-1)}\right\rangle + \left|T^{(+1)}\right\rangle\right) \\
\left|T^{(z)}\right\rangle &= \left|T^{(0)}\right\rangle
\end{aligned} \tag{14}$$

Alternatively, this first selection rule can be restated in terms of the eigenvectors in the perturbative expansion in Eqs. (4) and (5). In the first-order term, only wave functions belonging to the same representation as the zero-order wave function contribute to the spin-perturbed wave function. This approach is adopted by Marian in Ref. [8].

The second selection rule concerns the dipole moments in Eq. (7). The transition can only be allowed if at least one of the elements belongs to the totally symmetric representation:

$$\Gamma\left(\left\langle S_0 \left| \hat{\boldsymbol{\mu}} \right| S_L \right\rangle\right) \; or \; \Gamma\left(\left\langle T_K \left| \hat{\boldsymbol{\mu}} \right| T_1 \right\rangle\right) \supset \Gamma_1 \tag{15}$$

In this expression, a component $\hat{\xi}$ of a singlet-singlet transition dipole contributes to the phosphorescence if

$$\Gamma\left(\left|S_0\right\rangle\right)\Gamma\left(\left|S_L\right\rangle\right) = \Gamma\left(\hat{\xi}\right) \tag{16}$$

Alternatively, the component $\hat{\xi}$ of a triplet-triplet transition dipole contributes if

$$\Gamma\left(\left|T_K\right\rangle\right)\Gamma\left(\left|T_1\right\rangle\right) = \Gamma\left(\hat{\xi}\right) \tag{17}$$

These two selection rules are weak because the perturbative expansion sums over many *L* and *K* states. Thus, it is always likely that some states will satisfy them even for a highly symmetric structure. Physically, however, it is relevant whether the low-order terms satisfy the conditions or not since they contribute the most to the singlet-triplet transition dipole. Thus, for our analysis, we restrict the perturbative contributions in Eq. (6) to contain only S_0, S_1, T_1, and T_2 states (L = 0, 1 and K = 1, 2), reducing it to

$$\tilde{\boldsymbol{\mu}}_{10}^{(\xi)} \approx \frac{\left\langle \mathrm{T}_1^{(\xi)} \middle| \hat{H}^{SO} \middle| \mathrm{S}_0 \right\rangle}{{}^3E_1 - {}^1E_0} \left[\left\langle \mathrm{S}_0 \middle| \hat{\boldsymbol{\mu}} \middle| \mathrm{S}_0 \right\rangle - \left\langle \mathrm{T}_1 \middle| \hat{\boldsymbol{\mu}} \middle| \mathrm{T}_1 \right\rangle \right] + \frac{\left\langle \mathrm{T}_1^{(\xi)} \middle| \hat{H}^{SO} \middle| \mathrm{S}_1 \right\rangle}{{}^3E_1 - {}^1E_1} \left\langle \mathrm{S}_1 \middle| \hat{\boldsymbol{\mu}} \middle| \mathrm{S}_0 \right\rangle + \frac{\left\langle \mathrm{T}_2^{(\xi)} \middle| \hat{H}^{SO} \middle| \mathrm{S}_0 \right\rangle}{{}^1E_0 - {}^3E_2} \left\langle \mathrm{T}_1 \middle| \hat{\boldsymbol{\mu}} \middle| \mathrm{T}_2 \right\rangle \tag{18}$$

These three terms, corresponding to the three coupling mechanisms introduced in Section 2, are schematically illustrated in Figure 5. Because they have the smallest denominators in the series, they tend to dominate the qualitative features of the total transition dipole, even though the high-order terms are essential for the quantitative description.

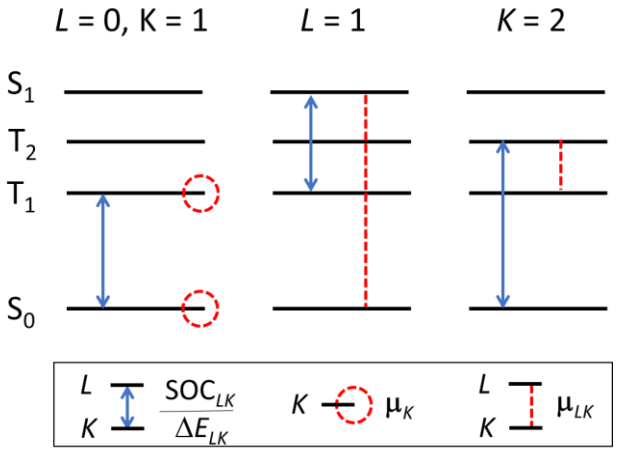

Figure 5. Each diagram illustrates one of the three terms in Eq. (18). The first is a direct SOC mechanism, the second is an indirect SOC-dipole mechanism, and the third is an indirect dipole-SOC mechanism. The double arrow indicates the SOC divided by the singlet-triplet energy difference; the dashed circle indicates a permanent dipole moment, and the dashed line is a transition dipole moment.

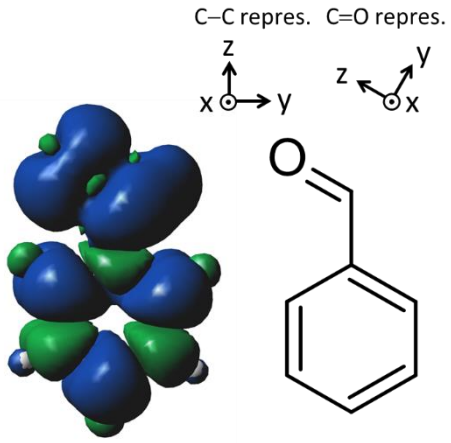

Figure 6. Spin density of the T_1 state of benzaldehyde (left). Two Cartesian axes are indicated, corresponding to the C–C and C=O representations.

Let us now apply these conditions to BA. Although the T_1 minimum has C_s symmetry, we should at least work with C_{2v} point group to be able to distinguish between allowed and forbidden matrix elements. The T_1 spin density shown in Figure 6 indicates that BA can be approximately treated as a C_{2v} system, with the principal axis either along the C–C direction or the C=O direction (see both representations in the figure).

We first assume that the principal axis is oriented along C–C. As discussed in the previous section, BA has two T_1 minima, with $^3n\pi^*$ (~B_1) and $^3\pi\pi^*$ (~A_1) characters (see excitations and molecular orbitals in SI-2). In both minima, S_0 is ~A_1 and S_1 is ~B_1 ($^1n\pi^*$). At the $^3n\pi^*$ minimum, T_2 is a $^3\pi\pi^*$ (~A_1) while at $^3\pi\pi^*$ minimum, T_2 is an $^3n\pi^*$ (~B_1). In C_{2v}, *x*, *y*, and *z* transform as B_1, B_2, and A_1, respectively. In turn, R_x, R_y, and R_z transform as B_2, B_1, and A_2, respectively.

For the $^3n\pi^*$ minimum, the first selection rule [Eqs. (13)] imposes that the only non-null SOC elements in Eq. (18) are $\left\langle T_1^{(y)} \middle| \hat{H}^{SO} \middle| S_0 \right\rangle$, appearing in the first term. (Applying Eq. (11), the symmetry of $T_1^{(y)}$ is $\Gamma(^3n\pi^*) \times \Gamma(R_y) = B_1 \times B_1 = A_1$.) Thus, the short expansion of the singlet-triplet transition dipole [Eq. (18)] simplifies to

$$\tilde{\boldsymbol{\mu}}_{n\pi^*\to S_0}^{(y)[\text{C-C}]} \approx \frac{\left\langle T_1^{(y)} \middle| \hat{H}^{SO} \middle| S_0 \right\rangle}{^3E_1 - {}^1E_0} \left[\left\langle S_0 \middle| \hat{\boldsymbol{\mu}} \middle| S_0 \right\rangle - \left\langle T_1 \middle| \hat{\boldsymbol{\mu}} \middle| T_1 \right\rangle \right] \tag{19}$$

corresponding to the direct SOC mechanism.

The second selection rule [Eq. (15)] limits the contribution to the *z* component of the permanent dipoles. Therefore, for the $^3n\pi^*$ minimum, emission occurs exclusively oriented along *z*,

$$\tilde{\mu}_{n\pi^*\to S_0}^{(y)[\text{C-C}]} \approx \frac{\left\langle T_1^{(y)} \middle| \hat{H}^{SO} \middle| S_0 \right\rangle}{^3E_1 - {}^1E_0} \left[\left\langle S_0 \middle| \hat{z} \middle| S_0 \right\rangle - \left\langle T_1 \middle| \hat{z} \middle| T_1 \right\rangle \right] \tag{20}$$

The singlet-triplet transition dipole moments considering the complete first-order perturbative expansion in C_{2v} are given in SI-5.

Comparatively, if we apply these selection rules to the $^3\pi\pi^*$ minimum, once more, only sublevel *y* has a non-null transition dipole in the short expansion, given by

$$\tilde{\mu}_{\pi\pi^*\to S_0}^{(y)[\text{C-C}]} \approx \frac{\left\langle T_1^{(y)} \middle| \hat{H}^{SO} \middle| S_1 \right\rangle}{^3E_1 - {}^1E_1} \left\langle S_1 \middle| \hat{x} \middle| S_0 \right\rangle + \frac{\left\langle T_2^{(y)} \middle| \hat{H}^{SO} \middle| S_0 \right\rangle}{^1E_0 - {}^3E_2} \left\langle T_1 \middle| \hat{x} \middle| T_2 \right\rangle \tag{21}$$

and oriented in the *x* direction. In this case, only the indirect SOC-dipole and dipole-SOC mechanisms contribute.

These results in Eqs. (20) and (21) explain why $^3n\pi^*\to S_0$ phosphorescence is so much faster than $^3\pi\pi^*\to S_0$ one for aromatic carbonyls. The spin SOC elements have similar magnitudes in both expressions (about 20 cm^{-1}). Nevertheless, the permanent dipoles in Eq. (20) are about 40 times bigger than the transition dipoles in Eq. (21) (SI-6).

Olmsted and El-Sayed proposed that BA phosphorescence could be analyzed using a C=O diatomic model [4]. Suppose we follow their suggestion and rotate the *z*-axis to coincide with the carbonyl bond direction, as in Refs. [3, 12]. The axes convention for this C=O representation are indicated in Figure 6. In that case, the approximated C_{2v} assignment of the states change ($\pi\pi^*$ and $n\pi^*$ become $\sim A_1$ and $\sim A_2$, respectively; see symmetry analysis in SI-2), but the conclusions above remain valid.

To see that, note that for the $^3n\pi^*$ ($\sim A_2$) T_1 minimum, T_2 $^3\pi\pi^*$ is $\sim A_1$ and S_1 $^1n\pi^*$ is $\sim A_2$. The second T_1 minimum is $^3\pi\pi^*$ ($\sim A_1$), where T_2 $^3n\pi^*$ is $\sim A_2$ and S_1 $^1n\pi^*$ is $\sim A_2$. S_0 is $\sim A_1$ in both minima. For the $^3n\pi^*$ minimum, the only non-null SOC term in the short expansion is in sublevel *z* with emission along *z* through the permanent dipole terms, that is

$$\tilde{\mu}_{10}^{(z)[\mathrm{C=O}]} \approx \frac{\left\langle \mathrm{T}_1^{(z)} \middle| \hat{H}^{SO} \middle| \mathrm{S}_0 \right\rangle}{{}^3E_1 - {}^1E_0} \left[\left\langle \mathrm{S}_0 \middle| \hat{z} \middle| \mathrm{S}_0 \right\rangle - \left\langle \mathrm{T}_1 \middle| \hat{z} \middle| \mathrm{T}_1 \right\rangle \right] \tag{22}$$

For the $^3\pi\pi^*$ minimum, the SOC term in the *z* sublevel is allowed in the indirect coupling terms. However, all transition dipole terms are forbidden in the short expansion, rendering a null singlet-triplet transition dipole moment from this state. Thus, once again, we obtained that emission from $^3n\pi^*$ should be faster than from $^3\pi\pi^*$.

In both symmetry orientations, the crucial distinction between $^3n\pi^*$ and $^3\pi\pi$ is their spatial symmetry, $\Gamma(^3\pi\pi^*) = \Gamma(S_0) = \Gamma_1$ while $\Gamma(^3n\pi^*) \neq \Gamma(S_0)$. For the C_{2v} and D_2 groups, for which $\Gamma(R_\xi) \neq \Gamma_1$, the first relation implies that $^3\pi\pi^*$ cannot satisfy the first selection rule [Eq. (13)] and $\left\langle {}^3\pi\pi^{*(\xi)} \middle| \hat{H}^{SO} \middle| \mathrm{S}_0 \right\rangle = 0$. Because these groups are Abelian with order 4, one of the Cartesian components ξ yields $\Gamma(^3n\pi^*)\,\Gamma(R_\xi) = \Gamma_1$. Therefore, they satisfy the first selection rule and give $\left\langle {}^3n\pi^{*(\xi)} \middle| \hat{H}^{SO} \middle| \mathrm{S}_0 \right\rangle \neq 0$.

For D_n ($n > 2$), C_{nv} ($n > 2$), D_{nh}, D_{nd}, and cubic groups, $\left\langle {}^3\pi\pi^{*(\xi)} \middle| \hat{H}^{SO} \middle| \mathrm{S}_0 \right\rangle = 0$ for the same reason, but we cannot guarantee that $\left\langle {}^3n\pi^{*(\xi)} \middle| \hat{H}^{SO} \middle| \mathrm{S}_0 \right\rangle \neq 0$. For C_n ($n > 2$), C_{nh}, and S_n, at least one $\Gamma(R_\xi)$ is Γ_1, and $\left\langle {}^3\pi\pi^{*(\xi)} \middle| \hat{H}^{SO} \middle| \mathrm{S}_0 \right\rangle \neq 0$ for these components. In principle, this is also the case for C_1, C_2, and C_s, but molecules belonging to these groups may have $\left\langle {}^3\pi\pi^{*(\xi)} \middle| \hat{H}^{SO} \middle| \mathrm{S}_0 \right\rangle \approx 0$, if they are close to C_{2v} (like BA is, for example). A survey of these conditions is given in Table 6.

The analysis in this section allows concluding that $^3n\pi^*$ phosphoresce will be much faster than $^3\pi\pi^*$ one if:

1. $^3\pi\pi^*$ is totally symmetric, and the molecule (at least approximately) attains C_{2v} or D_2 symmetry. It may also be valid for other point groups, as indicated in Table 6, but it depends on the specific irreducible representation of the states.
2. The difference between permanent dipole moments in the triplet and singlet states is much bigger than the transition dipole moments between singlets and between triplet states (which is a consequence of Eqs. (20) and (21)).

Table 6. Status of the first selection rule concerning the SOC matrix elements. ϕ and φ are the spatial configurations of the singlet and triplet states, respectively. $\Gamma(R_\xi)$ is the irreducible representation of the Cartesian rotation in ξ. If the spatial configurations of the singlet and triplet states in relation 1 are identical, this table corresponds to the El-Sayed rule.

	Relation 1 $\left\langle {}^1\phi \middle\vert \hat{H}^{SO} \middle\vert {}^3\varphi^{(\xi)} \right\rangle = 0$ with $\Gamma(\phi) = \Gamma(\varphi)$	Relation 2 $\left\langle {}^1\phi \middle\vert \hat{H}^{SO} \middle\vert {}^3\varphi^{(\xi)} \right\rangle \neq 0$ with $\Gamma(\phi) \neq \Gamma(\varphi)$
The relation is valid if:	$\Gamma(R_\xi) \neq \Gamma_1$ (all ξ)	$\Gamma(\varphi)\Gamma(R_\xi) = \Gamma(\phi)$ (at least one ξ)
Point group		
C_{2v}, D_2	True	True
D_n ($n > 2$), C_{nv} ($n > 2$), D_{nh}, D_{nd}, cubic groups	True	Not necessarily true
C_1, C_2, C_s	False	True
C_n ($n > 2$), C_{nh}, S_n	False	Not necessarily true

Note that the first point implies that if, for a C_{2v} molecule, the $^3\pi\pi^*$ state is B_2, its phosphorescence lifetime is not necessarily longer than that of a $^3n\pi^*$.

The phosphorescence polarization is (with the phosphorescence lifetime) another indicator of the emitting state character [60]. Experimentally, one expects a $^3n\pi^*$ emission in the molecular plane and a $^3\pi\pi^*$ emission perpendicular to the molecular plane [2, 61]. Eqs. (20) and (21) for C–C representation corroborate these emission directions, with $^3n\pi^*$ and $^3\pi\pi^*$ emissions polarized in the *z*- and *x*-directions, respectively. However, these polarization directions are only significantly preferential in $^3n\pi^*$, for which the permanent dipole terms dominate. $\tilde{T}_1^{(z)}$ emits polarized in *y*, but it is proportional to small transition dipole terms involving states beyond S_1 and T_2 (SI-5). In the $^3\pi\pi^*$ emission, perturbative terms in $\tilde{T}_1^{(x)}$ (also involving states beyond S_1 and T_2) introduce significant emission polarized along *y*. Similar conclusions are reached with the C=O representation. Although the triplet sublevel changes from *y* to *z* when changing from C–C to C=O representation, the emission is still primarily in plane, as shown in Eqs. (20) and (22).

5.2 Phosphorescence lifetime connection to the El-Sayed rule

The El-Sayed rule is often invoked to explain the difference between $^3n\pi^*$ and $^3\pi\pi^*$ phosphorescence lifetimes in aromatic carbonyls [11]. A possible source for this prevailing association between the El-Sayed rule and phosphorescence lifetime may be the 1971 paper by Olmsted and El-Sayed on benzaldehyde [4], where they claimed that "Most of the phosphorescence emission arises because of the direct spin-orbit interaction: $^3A''(n\pi^*) \overset{SOC}{\leftrightarrow} {}^1A'(\pi\pi^*)$," evoking the El-Sayed rule [56]. However, this specific SOC term (appearing in the $\left\langle T_1^{(m)} \middle\vert \hat{H}^{SO} \middle\vert S_2 \right\rangle \langle S_2 \vert \hat{\boldsymbol{\mu}} \vert S_0 \rangle \left({}^3E_1 - {}^1E_2 \right)^{-1}$ contribution of the singlet-triplet transition dipole moment [Eq. (7)]) should have a minor contribution.

In any case, is there a connection between the El-Sayed rule and the phosphorescence lifetimes? We anticipate that not unless we adopt a loose definition of the rule. Let us see the El-Sayed rule in the context and notation used in our work.

The El-Sayed rule states that the magnitude of the SOC matrix elements between triplet and singlet states with the same spatial configurations is much smaller than for states with different configurations [56]. It is rooted in the first selection rule discussed above [Eq. (13)], and we can express the El-Sayed rule as

$$\frac{\left|\sum_{\xi=x,y,z}\left\langle {}^1\phi\left|\hat{H}^{SO}\right|{}^3\phi^{(\xi)}\right\rangle\right|}{\left|\sum_{\xi=x,y,z}\left\langle {}^1\phi\left|\hat{H}^{SO}\right|{}^3\varphi^{(\xi)}\right\rangle\right|} \ll 1 \qquad (23)$$

where ϕ and φ represent the spatial configuration of the states. The validity of the El-Sayed rule for different point groups follows the conditions in Table 6. Thus, it is strictly valid for C_{2v} and D_2 molecules only. It may occasionally be valid for D_n ($n > 2$), C_{nv} ($n > 2$), D_{nh}, D_{nd}, and cubic groups, depending on the particular state's irreducible representations. Depending on how close the molecule is to a higher symmetry group, it may be approximately invoked for C_1, C_2, and C_s groups.

The El-Sayed rule is distinct from the rule we discussed in Section 5.1 because it imposes restrictions on the spatial configurations ϕ and φ, which are not required when discussing the phosphorescence lifetime. However, the El-Sayed rule is a particular case of the discussion in Section 5.1.

We started this subsection by asking whether there was a connection between the El-Sayed rule and the phosphorescence lifetimes. The difference between phosphorescence lifetimes depends on a SOC selection rule that is slightly more general than the El-Sayed rule, as it does impose any restriction on the spatial configurations. Moreover, the phosphorescence lifetimes also depend on the singlet-triplet dipole moment difference. Therefore, it seems inadequate to attribute the phosphorescence lifetime difference to a consequence of the El-Sayed rule.

5.3 Contributions for phosphorescence

The previous sections focused on the phosphorescence from the T_1 minimum geometry. However, the vibrational freedom allows vibronic couplings that may impact the emission. We have seen in Section 4.4 that how strongly they impact depends on the molecule and state character. For all molecules, vibronic couplings increased the $^3n\pi^*$ phosphorescence lifetime by about 20% (Table 5). On the other hand, vibronic coupling reduced the $^3\pi\pi^*$ phosphorescence lifetime by a factor of 32 in MoBA, 39 in MeBA, and 50 in DMABA, causing all three molecules to have similar vibronically corrected lifetimes of about 200 ms.

We can understand the vibronic contributions by looking at the three mechanisms composing the singlet-triplet transition dipole moment in Eq. (7). Figure 7 shows the contributions of each of these mechanisms to the singlet-triplet oscillator strength for emission from the lowest T_1 minimum of BA ($^3n\pi^*$), MeBA ($^3n\pi^*$), MoBA ($^3\pi\pi^*$), and DMABA ($^3\pi\pi^*$). The first row of graphs contains the final oscillator strength computed with Eq. (9). The next three rows have the oscillator strength

$$\tilde{f}_X = \frac{2m_e}{3\hbar^2 e^2}\Delta E_{10}\tilde{M}_X^2 \tag{24}$$

where $\tilde{M}_X^2 = \frac{1}{3}\sum_\alpha \left|\tilde{\mathbf{M}}_X^{(\alpha)}\right|^2$ is the partial triplet-singlet transition dipole moment for the direct SOC (DS), indirect SOC-dipole (ISD), and indirect dipole-SOC (IDS) mechanisms, computed respectively as

$$\begin{aligned}
\tilde{\mathbf{M}}_{DS}^{(\alpha)} &= \frac{\left\langle \mathrm{T}_1^{(\alpha)} \middle| \hat{H}^{SO} \middle| \mathrm{S}_0 \right\rangle}{{}^3E_1 - {}^1E_0}\left[\left\langle \mathrm{S}_0 \middle| \hat{\boldsymbol{\mu}} \middle| \mathrm{S}_0 \right\rangle - \left\langle \mathrm{T}_1 \middle| \hat{\boldsymbol{\mu}} \middle| \mathrm{T}_1 \right\rangle\right] \\
\tilde{\mathbf{M}}_{ISD}^{(\alpha)} &= \sum_{L\neq 0}^{\{\text{singlets}\}} \frac{\left\langle \mathrm{T}_1^{(\alpha)} \middle| \hat{H}^{SO} \middle| \mathrm{S}_L \right\rangle}{{}^3E_1 - {}^1E_L}\left\langle \mathrm{S}_L \middle| \hat{\boldsymbol{\mu}} \middle| \mathrm{S}_0 \right\rangle \\
\tilde{\mathbf{M}}_{IDS}^{(\alpha)} &= \sum_{L\neq 0}^{\{\text{singlets}\}} \frac{\left\langle \mathrm{T}_1^{(\alpha)} \middle| \hat{H}^{SO} \middle| \mathrm{S}_L \right\rangle}{{}^3E_1 - {}^1E_L}\left\langle \mathrm{S}_L \middle| \hat{\boldsymbol{\mu}} \middle| \mathrm{S}_0 \right\rangle
\end{aligned} \tag{25}$$

The histograms give the oscillator strength distribution of all points in the nuclear ensemble. The vertical and horizontal solid lines in each graph indicate the mean value and standard deviation for the distributions, respectively. The vertical dashed line marks the vertical oscillator strength in each case. The mean and vertical values are also collected in Table 7. The analysis, in terms of partial contributions, neglects crossing terms between mechanisms. Thus, the sum over DS, ISD, and IDS should not recover the total oscillator strength.

The total oscillator strength distributions (first row in Figure 7) show that BA and MeBA, with a $^3n\pi^*$ T_1 minimum, have NEA distributions with a broad peak with a non-null maximum. As expected, the vertical and NEA mean value oscillator strengths are similar, implying that the nuclear ensemble distributes around the $^3n\pi^*$ minimum. The distribution shows a second narrow peak at zero for both molecules, meaning that the ensemble also partially covers the $^3\pi\pi^*$ region.

MoBA and DMABA, with a $^3\pi\pi^*$ T_1 minimum, have total oscillator strength distributions peaked at zero. Again, this is the expected result, as the ensemble distributes around a minimum with near-zero vertical oscillator strength. The NEA mean value is significatively displaced toward larger oscillator strengths, reflecting the vibronic coupling introduced by the procedure.

As we have seen in Eq. (20), a molecule with a $^3n\pi^*$ T_1 minimum is expected to have dominant vertical contributions from the direct SOC mechanism and minor contributions from the indirect SOC-dipole and dipole-SOC mechanisms in the minimum geometry. This is precisely what the second, third, and fourth rows in Figure 7 reveal for BA and MeBA. Direct SOC dominates. The

indirect SOC-dipole mechanism has significant contributions, while the indirect dipole-SOC contribution is almost negligible.

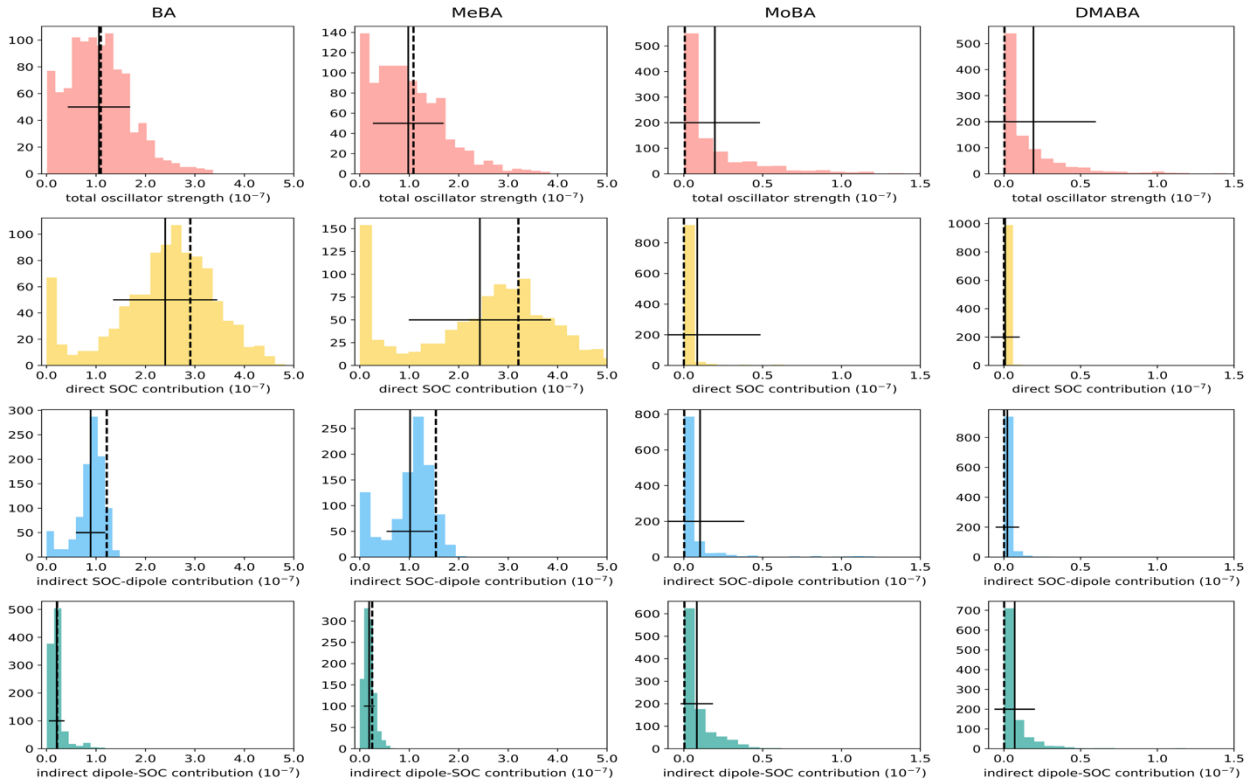

Figure 7. Histogram of the oscillator strengths and the individual contributions to the oscillator strengths of the three mechanisms in Eq. (7) for BA and its derivatives in the NEA simulations estimated with Eqs. (24) and (25). The first row shows the total oscillator strength. The second row corresponds to the direct SOC mechanism, while the third and fourth rows show the indirect SOC-dipole and dipole-SOC mechanisms, respectively. The black dashed vertical lines indicate the vertical value. The mean value and the standard deviation of each distribution are depicted by vertical and horizontal solid black lines, respectively. The values in the horizontal axes are dimensionless quantities, whereas the vertical axes show the counts. Crossing terms contributing to the transition dipole are neglected. All results include 20 singlet and 20 triplet states in the perturbative expansion.

The contributions to the singlet-triplet oscillator strength distributions are completely distinct when considering MoBA and DMABA. Both molecules have $^3\pi\pi^*$ T_1 minima; direct SOC should not contribute, as we can see in Eq. (21). The vertical contributions are nearly null for all three terms in Figure 7, explaining the 6.87 s and 11.5 s long phosphorescence lifetimes of MoBA and DMBA, respectively (Table 5). Note, however, that when vibronic couplings are introduced via NEA, the contributions from the three mechanisms increase significantly. As a result, the NEA phosphorescence lifetime drops to 213 ms in MoBA and 231 ms in DMABA, revealing a remarkable vibronic effect. As shown in Table 7, direct and indirect couplings contribute equally to the oscillator strength in MoBA and DMABA.

Table 7. Vertical and NEA mean contributions of each coupling mechanism to the singlet-triplet oscillator strength. These quantities, computed with Eqs. (24) and (25), give only an approximate estimate of the

importance of each mechanism, as they neglect crossing terms contributing to the total oscillator strength (also shown).

Molecule		Oscillator strength ($\times 10^{-7}$)			
		direct SOC	indirect SOC-dipole	indirect dipole-SOC	Total
BA (^{3}nπ*)	vertical	2.91	1.22	0.21	1.09
	NEA mean	2.40	0.89	0.21	1.06
MeBA (^{3}nπ*)	vertical	3.21	1.54	0.25	1.08
	NEA mean	2.43	1.02	0.19	0.98
MoBA (^{3}ππ*)	vertical	0.0000	0.0024	0.0034	0.0059
	NEA mean	0.0846	0.1027	0.0822	0.1964
DMABA (^{3}ππ*)	vertical	0.0000	0.0008	0.0015	0.0036
	NEA mean	0.0081	0.0226	0.0700	0.1925

6 Conclusions

This work analyzed the phosphorescence lifetime of aromatic carbonyl compounds. We aimed to explain the difference between ^{3}nπ* and ^{3}ππ* emissions and estimate the importance of vibronic contributions. We addressed these questions by combining formal analysis of the selection rules controlling the singlet-triplet transition dipole moments and simulating vertical and vibronically-corrected phosphorescence lifetimes for benzaldehyde (BA) and three derivatives (MeBA, MoBA, and DMABA). These systems range from ^{3}nπ* to ^{3}ππ* T_1 minimum, enabling a broad assessment of the different coupling mechanisms contributing to light emission.

It is well established that phosphorescence in aromatic carbonyls occurs within a few ms when T_1 has a ^{3}nπ* character, but it may take much longer when this state is a ^{3}ππ*. We explained this effect based on analyzing the first-order perturbative expansion of triplet-singlet transition dipole moments without considering vibronic couplings. We showed that the ^{3}nπ*-S_0 transition dipole moment depends on the permanent dipoles of the unperturbed S_0 and T_1, making it much bigger than the ^{3}ππ*-S_0 transition dipole moment, which depends on weaker transition dipole terms between unperturbed states.

This cause, however, is symmetry dependent. It is strictly valid only for molecules with C_{2v} and D_2 symmetries, although it can be approximately extended to other point groups. Moreover, it requires the ^{3}ππ* to be totally symmetric. Therefore, while our analysis clearly explains the phosphorescence lifetime difference between a ^{3}nπ* and a ^{3}ππ*(A_1) emission, we have no reason to expect that the phosphorescence lifetimes of a ^{3}nπ* and a ^{3}ππ*(B_2) emission would significantly differ. We additionally show that the difference in the phosphorescence lifetimes is not explained by the El-Sayed rule, as sometimes stated, although it is connected to it.

We estimated vertical and vibronically corrected phosphorescence lifetimes for BA, MeBA, MoBA, and DMABA using TDDFT. The vertical values predict $^3n\pi^*$ emission within 38 to 61 ms and $^3\pi\pi^*$ emission within 8 to 11 s, depending on the molecule (Table 5). Vibronic coupling introduced through the NEA approach increases the vertical $^3n\pi^*$ emission to 46 to 75 ms and drastically reduces the $^3\pi\pi^*$ emission to 214 to 231 ms. Although our results for the $^3n\pi^*$ seem to overestimate the lifetime, they deliver an excellent qualitative picture, where the $^3\pi\pi^*$ emission takes three to five times longer than the $^3n\pi^*$ emission. Based on experimental analysis of aromatic carbonyls, Harrigan and Hirota [3] proposed that this ratio should be about five times or bigger.

The TDDFT estimates of the phosphorescence lifetimes also corroborate our formal analysis of the reason for the lifetime difference. Decomposing the computed triplet-singlet oscillator strength in the three basic coupling mechanisms confirmed that within the vertical approximation, the direct SOC mechanism (proportional to the permanent dipole of unperturbed states) dominates $^3n\pi^*$ emissions and is absent in $^3\pi\pi^*$ emissions, as predicted by the formal analysis. This fact is especially significant considering that the aromatic carbonyls studied here have only a roughly approximated C_{2v} symmetry. Including vibronic couplings does not change this picture for $^3n\pi^*$ emissions but impacts $^3\pi\pi^*$ emissions by allowing direct and indirect coupling mechanisms to contribute equally.

The theoretical and experimental records about the phosphorescence lifetime of aromatic carbonyls are profoundly incomplete, which has been a problem for our analysis. At this point, we can only draw recommendations for future work in the field. On the theory side, applying other vibronic-coupling approaches with more accurate electronic structure methods to estimate aromatic carbonyls' phosphorescence lifetime would be helpful. Such results would allow for gauging the quality of the NEA predictions and explain the lifetime overestimation. Moreover, new theoretical studies could also expand the ensemble of molecules to check which kind of chemical functionalization could extend or reduce the $^3\pi\pi^*$ phosphorescence lifetimes.

On the experimental side, a systematic study of aromatic carbonyl phosphorescence using modern spectroscopic techniques and controlled conditions could help elucidate the true extent of the $^3n\pi^*$ and $^3\pi\pi^*$ lifetime differences.

Acknowledgments

SM, MK, and MB thank the support of the funding provided by European Research Council (ERC) Advanced grant SubNano (Grant agreement 832237). XG thanks the National Natural Science Foundation of China, grant No. 22273122.

Data availability

The datasets generated during the current study are available in figshare repository, Ref. [62]. They include the Cartesian coordinate of stationary structures and the raw data of the NEA simulations. The NEA phosphorescence method was implemented in Newton-X and is publicly available at www.newtonx.org. PySOC is freely available at gitlab.com/light-and-molecules/pysoc.

Author Contribution

Conceptualization: MB; Formal Analysis: SM, MB; Funding acquisition: MB; Investigation: SM, MK, MB; Methodology: XG, MB; Project administration: MB; Software: SM, MBh; Supervision: MB; Visualization: SM, MB; Writing – original draft: SM, MB; Writing – review & editing: SM, MBh, XG, MB.

Competing Interests

The authors have no relevant financial or non-financial interests to disclose.

References

1. Harrigan ET, Hirota N (1976) Microwave-induced delayed phosphorescence studies of the total and radiationless decay processes of $^3\pi\pi^*$ aromatic carbonyls. Mol Phys 31: 663-680 https://doi.org/10.1080/00268977600100521
2. Lower SK, El-Sayed MA (1966) The Triplet State and Molecular Electronic Processes in Organic Molecules. Chem Rev 66: 199-241 https://doi.org/10.1021/cr60240a004
3. Harrigan ET, Hirota N (1976) Phosphorescence microwave double resonance and spectroscopic studies of the radiative mechanisms of benzaldehyde type $^3\pi\pi^*$ aromatic carbonyls. Mol Phys 31: 681-697 https://doi.org/10.1080/00268977600100531
4. Olmsted J, El-Sayed MA (1971) Phosphorescence spectrum and mechanisms of benzaldehyde in methyl-cyclohexane at 4.2°K. J Mol Spectrosc 40: 71-83 https://doi.org/10.1016/0022-2852(71)90009-9
5. Zwarich RJ, Goodman L (1970) Out-of-plane vibrations in $T(n\pi^*) \rightarrow S_0$ of benzaldehyde. Chem Phys Lett 7: 609-611 https://doi.org/10.1016/0009-2614(70)87018-X
6. Zhao W, He Z, Lam Jacky WY, Peng Q, Ma H, Shuai Z, Bai G, Hao J, Tang Ben Z (2016) Rational Molecular Design for Achieving Persistent and Efficient Pure Organic Room-Temperature Phosphorescence. Chem 1: 592-602 https://doi.org/10.1016/j.chempr.2016.08.010
7. McGlynn SP, Azumi T, Kinoshita M (1969) Molecular spectroscopy of the triplet state. Prentice-Hall, New Jersey
8. Marian CM (2001) Reviews in Computational Chemistry. John Wiley & Sons, Inc. https://doi.org/10.1002/0471224413.ch3
9. Clementi E, Kasha M (1958) Spin-orbital interaction in N-heterocyclic molecules general results in a cylindrical potential approximation. J Mol Spectrosc 2: 297-307 https://doi.org/10.1016/0022-2852(58)90082-1
10. Sidman JW (1958) Spin-orbit coupling in pyrazine. J Mol Spectrosc 2: 333-341

https://doi.org/10.1016/0022-2852(58)90085-7
11. Anslyn EV, Dougherty DA (2006) Modern Physical Organic Chemistry. University Science Books
12. Cheng TH, Hirota N (1974) PMDR studies of the magnetic and dynamic properties of the lowest excited triplet states of aromatic carbonyl molecules: acetophenone, benzaldehyde and their derivatives. Mol Phys 27: 281-307
https://doi.org/10.1080/00268977400100291
13. Hilborn RC (1982) Einstein Coefficients, Cross-Sections, *f* Values, Dipole-Moments, and All That. Am J Phys 50: 982-986
https://doi.org/10.1119/1.12937
14. Baryshnikov G, Minaev B, Ågren H (2017) Theory and Calculation of the Phosphorescence Phenomenon. Chem Rev 117: 6500-6537
https://doi.org/10.1021/acs.chemrev.7b00060
15. Peng Q, Niu Y, Shi Q, Gao X, Shuai Z (2013) Correlation Function Formalism for Triplet Excited State Decay: Combined Spin–Orbit and Nonadiabatic Couplings. J Chem Theory Comput 9: 1132-1143
https://doi.org/10.1021/ct300798t
16. Minaev B, Baryshnikov G, Agren H (2014) Principles of phosphorescent organic light emitting devices. PCCP 16: 1719-1758
https://doi.org/10.1039/C3CP53806K
17. Jansson E, Norman P, Minaev B, Ågren H (2006) Evaluation of low-scaling methods for calculation of phosphorescence parameters. J Chem Phys 124: 114106
https://doi.org/10.1063/1.2179432
18. Crespo-Otero R, Barbatti M (2012) Spectrum Simulation and Decomposition with Nuclear Ensemble: Formal Derivation and Application to Benzene, Furan and 2-Phenylfuran. Theor Chem Acc 131: 1237
https://doi.org/10.1007/s00214-012-1237-4
19. Rocha AB, Bielschowsky CE (2000) Vibronic coupling for H_2CO and CO_2. Chem Phys 253: 51-57
https://doi.org/10.1016/S0301-0104(99)00379-1
20. Santoro F, Jacquemin D (2016) Going beyond the vertical approximation with time-dependent density functional theory. WIREs: Comp Mol Sci 6: 460-486
https://doi.org/10.1002/wcms.1260
21. de Souza B, Neese F, Izsák R (2018) On the theoretical prediction of fluorescence rates from first principles using the path integral approach. J Chem Phys 148: 034104
https://doi.org/10.1063/1.5010895
22. Torres AD, de Moura CEV, Oliveira RR, Rocha AB (2022) Comparison among several vibronic coupling methods. J Mol Model 28: 253
https://doi.org/10.1007/s00894-022-05230-8
23. Arbelo-González W, Crespo-Otero R, Barbatti M (2016) Steady and Time-Resolved Photoelectron Spectra Based on Nuclear Ensembles. J Chem Theory Comput 12: 5037-5049
https://doi.org/10.1021/acs.jctc.6b00704
24. Barbatti M, Bondanza M, Crespo-Otero R, Demoulin B, Dral PO, Granucci G, Kossoski F, Lischka H, Mennucci B, Mukherjee S, Pederzoli M, Persico M, Pinheiro Jr M, Pittner J, Plasser F, Sangiogo Gil E, Stojanovic L (2022) Newton-X Platform: New Software Developments for Surface Hopping and Nuclear Ensembles. J Chem Theory Comput 18: 6851-6865
https://doi.org/10.1021/acs.jctc.2c00804

25. Petit AS, Subotnik JE (2014) How to calculate linear absorption spectra with lifetime broadening using fewest switches surface hopping trajectories: A simple generalization of ground-state Kubo theory. J Chem Phys 141: 014107
https://doi.org/10.1063/1.4884945
26. Xue B-X, Barbatti M, Dral PO (2020) Machine Learning for Absorption Cross Sections. J Phys Chem A 124: 7199-7210
https://doi.org/10.1021/acs.jpca.0c05310
27. Biron M, Longin P (1985) Triplet dynamics of gas-phase benzaldehyde after excitation of the forbidden $T_1(n, \pi^*) \leftarrow S_0$ transition. Chem Phys Lett 116: 250-253
https://doi.org/10.1016/0009-2614(85)80163-9
28. Inoue A, Ebara N (1984) Triplet dynamics of benzaldehyde as studied by electron impact excitation. Chem Phys Lett 109: 27-30
https://doi.org/10.1016/0009-2614(84)85394-4
29. Brühlmann U, Nonella M, Russegger P, Huber JR (1983) The triplet state decay ($T_1(n\pi^*) \rightarrow S_0$) of benzaldehydes in the dilute gas phase. Chem Phys 81: 439-447
https://doi.org/10.1016/0301-0104(83)85335-X
30. Hirata Y, Lim EC (1980) Nonradiative electronic relaxation of gas phase aromatic carbonyl compounds: Benzaldehyde. J Chem Phys 72: 5505-5510
https://doi.org/10.1063/1.438967
31. Itoh T, Takemura T, Baba H (1976) Excitation-energy dependence of phosphorescence quantum yield of benzaldehyde vapour at low pressure. Chem Phys Lett 40: 481-483
https://doi.org/10.1016/0009-2614(76)85123-8
32. Itoh T (1988) The evidence showing that the intersystem crossing yield of benzaldehyde vapour is unity. Chem Phys Lett 151: 166-168
https://doi.org/10.1016/0009-2614(88)80089-7
33. Koyanagi M, Goodman L (1971) Triplet State of Benzaldehyde. J Chem Phys 55: 2959-2976
https://doi.org/10.1063/1.1676523
34. Bagnich SA (1998) Long-lived luminescence of complex molecules. J Appl Spectrosc 65: 687-700
https://doi.org/10.1007/BF02679842
35. Hossain M, Hanson DM (1978) Relative magnitudes of singlet and triplet state dipole moments: the lowest nπ* excited states of p-methylbenzaldehyde and p-chlorobenzaldehyde. Chem Phys 30: 155-161
https://doi.org/10.1016/0301-0104(78)85115-5
36. Feenstra JS, Park ST, Zewail AH (2005) Excited state molecular structures and reactions directly determined by ultrafast electron diffraction. J Chem Phys 123: 221104
https://doi.org/10.1063/1.2140700
37. Ohmori N, Suzuki T, Ito M (1988) Why does intersystem crossing occur in isolated molecules of benzaldehyde, acetophenone, and benzophenone? J Phys Chem 92: 1086-1093
https://doi.org/10.1021/j100316a019
38. Cui G, Lu Y, Thiel W (2012) Electronic excitation energies, three-state intersections, and photodissociation mechanisms of benzaldehyde and acetophenone. Chem Phys Lett 537: 21-26
https://doi.org/10.1016/j.cplett.2012.04.008
39. Zhao H, Zhang Y, Zhao Q, Li Y, Huang Z (2022) A Theoretical Study of H-Abstractions of Benzaldehyde by H, $O_3(P)$, $^3O_2$, OH, HO_2, and CH_3 Radicals: Ab Initio Rate Coefficients and Their Uncertainty Quantification. J Phys Chem A 126: 7523-7533
https://doi.org/10.1021/acs.jpca.2c02384

40. Ou Q, Subotnik JE (2013) Electronic Relaxation in Benzaldehyde Evaluated via TD-DFT and Localized Diabatization: Intersystem Crossings, Conical Intersections, and Phosphorescence. J Phys Chem C 117: 19839-19849
https://doi.org/10.1021/jp405574q
41. Yang N-C, McClure DS, Murov S, Houser JJ, Dusenbery R (1967) Photoreduction of acetophenone and substituted acetophenones. J Am Chem Soc 89: 5466-5468
https://doi.org/10.1021/ja00997a037
42. Berger M, Goldblatt IL, Steel C (1973) Photochemistry of benzaldehyde. J Am Chem Soc 95: 1717-1725
https://doi.org/10.1021/ja00787a004
43. Itoh T (1989) Photophysics and photochemistry of anisaldehyde vapor. J Photochem Photobiol A 50: 171-181
https://doi.org/10.1016/1010-6030(89)85013-0
44. Itoh T (2003) The lowest excited triplet (T_1) energies of p-methoxybenzaldehyde and p-cyanobenzaldehyde vapors estimated from the temperature dependence of the $T_2(n, \pi^*)$ phosphorescence and the $S_1(n, \pi^*)$ fluorescence spectra. Spectrochim Acta A Mol Biomol Spectrosc 59: 61-68
https://doi.org/10.1016/S1386-1425(02)00145-2
45. Stephens PJ, Devlin FJ, Chabalowski CF, Frisch MJ (1994) Ab Initio Calculation of Vibrational Absorption and Circular Dichroism Spectra Using Density Functional Force Fields. J Phys Chem 98: 11623-11627
https://doi.org/10.1021/j100096a001
46. Hehre WJ, Ditchfield R, Pople JA (1972) Self-Consistent Molecular-Orbital Methods. XII. Further Extensions of Gaussian-Type Basis Sets for Use in Molecular-Orbital Studies of Organic-Molecules. J Chem Phys 56: 2257-2261
https://doi.org/10.1063/1.1677527
47. Casida M (1995) In: Chong D (ed) Recent advances in density functional methods, Part I. World Scientific, Singapore
https://doi.org/10.1142/2914
48. Yanai T, Tew DP, Handy NC (2004) A New Hybrid Exchange-Correlation Functional Using the Coulomb-Attenuating Method (CAM-B3LYP). Chem Phys Lett 393: 51-57
https://doi.org/10.1016/j.cplett.2004.06.011
49. Chai J-D, Head-Gordon M (2008) Systematic Optimization of Long-Range Corrected Hybrid Density Functionals. J Chem Phys 128: 084106-084115
https://doi.org/10.1063/1.2834918
50. Sears JS, Koerzdoerfer T, Zhang C-R, Brédas J-L (2011) Communication: Orbital instabilities and triplet states from time-dependent density functional theory and long-range corrected functionals. J Chem Phys 135: 151103
https://doi.org/10.1063/1.3656734
51. Gao X, Bai S, Fazzi D, Niehaus T, Barbatti M, Thiel W (2017) Evaluation of Spin-Orbit Couplings with Linear-Response Time-Dependent Density Functional Methods. J Chem Theory Comput 13: 515-524
https://doi.org/10.1021/acs.jctc.6b00915
52. Marian CM (2012) Spin–orbit coupling and intersystem crossing in molecules. WIREs: Comp Mol Sci 2: 187-203
https://doi.org/10.1002/wcms.83
53. Frisch MJ, Trucks GW, Schlegel HB, Scuseria GE, Robb MA, Cheeseman JR, Scalmani G, Barone V, Petersson GA, Nakatsuji H, Li X, Caricato M, Marenich AV, Bloino J, Janesko BG, Gomperts R, Mennucci B, Hratchian HP, Ortiz JV, Izmaylov AF, Sonnenberg JL, Williams-Young D, Ding F, Lipparini F, Egidi F, Goings J, Peng B, Petrone A, Henderson T,

Ranasinghe D, Zakrzewski VG, Gao J, Rega N, Zheng G, Liang W, Hada M, Ehara M, Toyota K, Fukuda R, Hasegawa J, Ishida M, Nakajima T, Honda Y, Kitao O, Nakai H, Vreven T, Throssell K, Montgomery Jr. JA, Peralta JE, Ogliaro F, Bearpark MJ, Heyd JJ, Brothers EN, Kudin KN, Staroverov VN, Keith TA, Kobayashi R, Normand J, Raghavachari K, Rendell AP, Burant JC, Iyengar SS, Tomasi J, Cossi M, Millam JM, Klene M, Adamo C, Cammi R, Ochterski JW, Martin RL, Morokuma K, Farkas O, Foresman JB, Fox DJ (2016) *Gaussian 16 Rev. C.01*, Wallingford, CT
https://gaussian.com

54. Chiodo SG, Leopoldini M (2014) MolSOC: A spin–orbit coupling code. Comput Phys Commun 185: 676-683
https://doi.org/10.1016/j.cpc.2013.10.014

55. Molina V, Merchán M (2001) Theoretical Analysis of the Electronic Spectra of Benzaldehyde. J Phys Chem A 105: 3745-3751
https://doi.org/10.1021/jp004041t

56. El-Sayed MA (1963) Spin-Orbit Coupling and the Radiationless Processes in Nitrogen Heterocyclics. J Chem Phys 38: 2834-2838
https://doi.org/10.1063/1.1733610

57. Takemura T, Baba H (1969) Effects of Substitution on the Phosphorescence Process of Aromatic Carbonyl Compounds. Bull Chem Soc Jpn 42: 2756-2762
https://doi.org/10.1246/bcsj.42.2756

58. Franco de Carvalho F, Curchod BFE, Penfold TJ, Tavernelli I (2014) Derivation of Spin-Orbit Couplings in Collinear Linear-Response TDDFT: A Rigorous Formulation. J Chem Phys 140: 144103
https://doi.org/doi:http://dx.doi.org/10.1063/1.4870010

59. Huix-Rotllant M, Ferré N, Barbatti M (2020) In: González L, Lindh R (eds) Quantum Chemistry and Dynamics of Excited States: Methods and Applications. John Wiley & Sons
https://doi.org/10.1002/9781119417774.ch2

60. Lin Z-P, Aue WA (2000) Gas-phase luminescence of aromatic carbonyl compounds in excited nitrogen at atmospheric pressure. Can J Chem 78: 95-117
https://doi.org/10.1139/v99-203

61. Shimada R, Goodman L (1965) Polarization of Aromatic Carbonyl Spectra. J Chem Phys 43: 2027-2041
https://doi.org/10.1063/1.1697070

62. Mukherjee S, Kar M, Bhati M, Gao X, Barbatti M (2023). figshare
https://doi.org/10.6084/m9.figshare.22277548.v2